Supporting information

Oxygen-Intercalated Ruddlesden-Popper Nickelate:

Giant Resistive Switching and Emergent Multi-Electronic Phase Control

Yufei Yao[1,#], Yanan Zhao[1,#,], Ping Li[1,#], Jie Zou[1], Zhilu Ye[1], Xuhui Zhu[1], Guannan Yang[1], Shishun Zhao[1], Guohua Dong[1], Bin Peng[1], Qian Li[2], Zhixin Guo[1,*], and Ming Liu[1,*]*

1.Electronic Materials Research Laboratory, Key Laboratory of the Ministry of Education & International Center for Dielectric Research, School of Electronic Science and Engineering, State Key Laboratory for Manufacturing Systems Engineering, Collaborative Innovation Center of High-End Manufacturing Equipment, Xi'an Jiaotong University, Xi'an 710049, China
2.National Synchrotron Radiation Laboratory and School of Nuclear Science and Technology, University of Science and Technology of China, Hefei, Anhui 230026, China

Part One: Other supporting experimental results

(1) Strain engineering $NdNiO_3$ based on different substrates

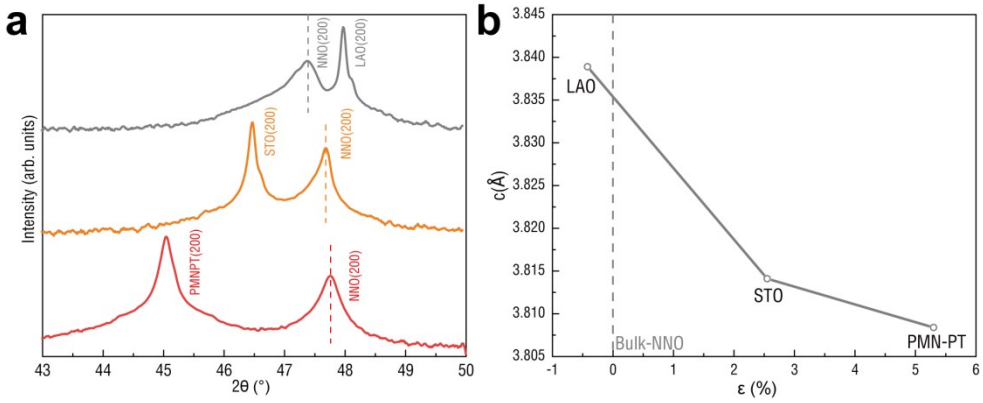

Figure S1 Heteroepitaxial growth of $NdNiO_3$ thin films. (a) The X-ray diffraction peaks, showing the (002) Bragg reflections. (b) The variation trend of lattice constant in c direction with strain..

Epitaxial $NdNiO_3$ thin films were deposited on singlecrystal $LaAlO_3$ (LAO), $SrTiO_3$ (STO) and $(PbMg_{0.33}Nb_{0.67})_{1-x}$: $(PbTiO_3)_x$ (PMN-PT) substrates by pulsed laser ablation of a single-phase target. The (002) X-ray diffraction peak shifts toward a larger angle (Figure S1a), indicating the lattice constant in c direction decreases with the increase of strain from the substrate.

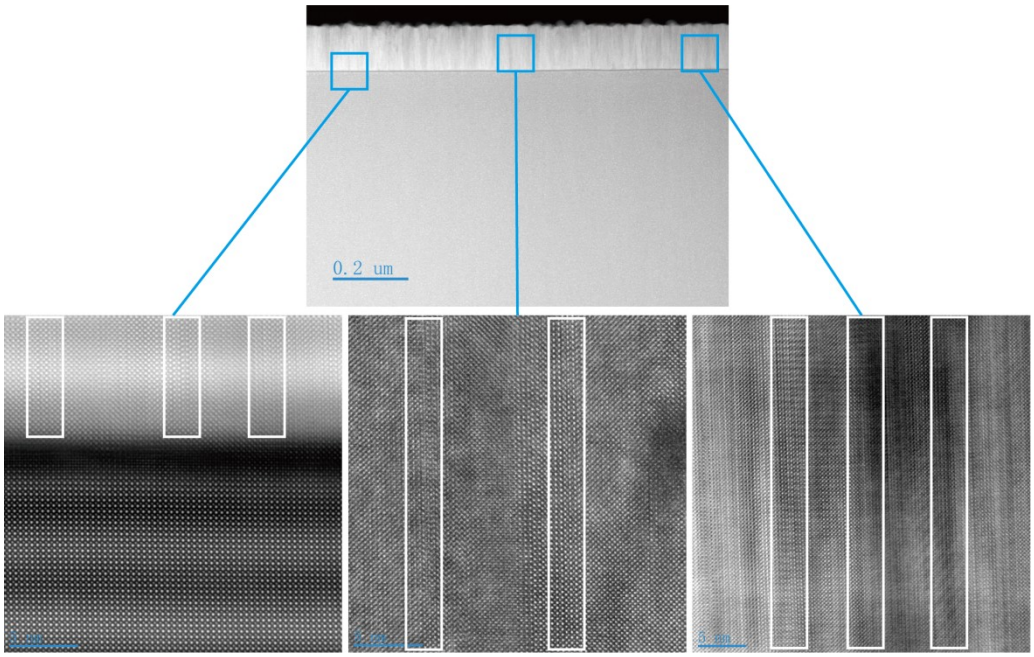

Figure S2 Atomic-resolution image of R.P. $(NdNiO_3)_n$:NdO films in the a-c plane, and blue block diagrams represent different regions. Here, white blocks represent the R.P.phase region.

As shown in Figure S2, the large tensile stress (ε=5.3%) induces a high-density formation of R.P. phases, where the R.P. $(NdNiO_3)_n$:NdO films are mainly observed in regions marked as white block.

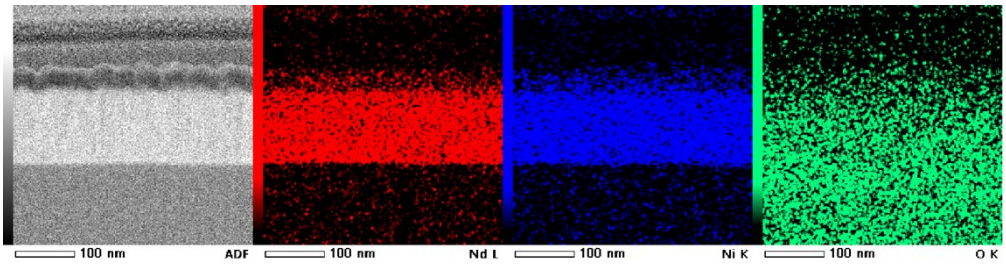

Figure S3 Low-magnification Z-contrast image of the R.P. $(NdNiO_3)_n$:NdO , and EDS maps corresponding to the Nd *L*, Ni *K*, O *K* edges are shown.

As shown in Figure S3, the clear boundary is between different elements in the film section.

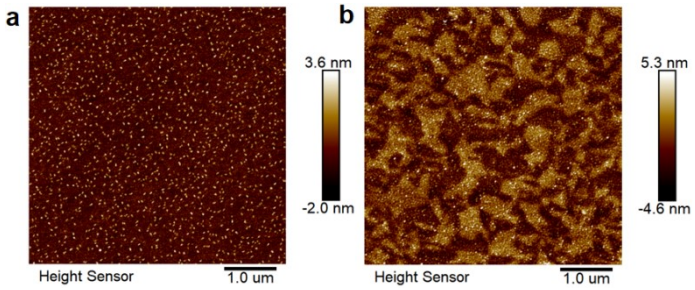

Figure S4 The surface topographic images acquired by atomic force microscopy reveal surface morphology of the (a)perovskite $NdNiO_3$ and (b)R.P. $(NdNiO_3)_n$:NdO films.

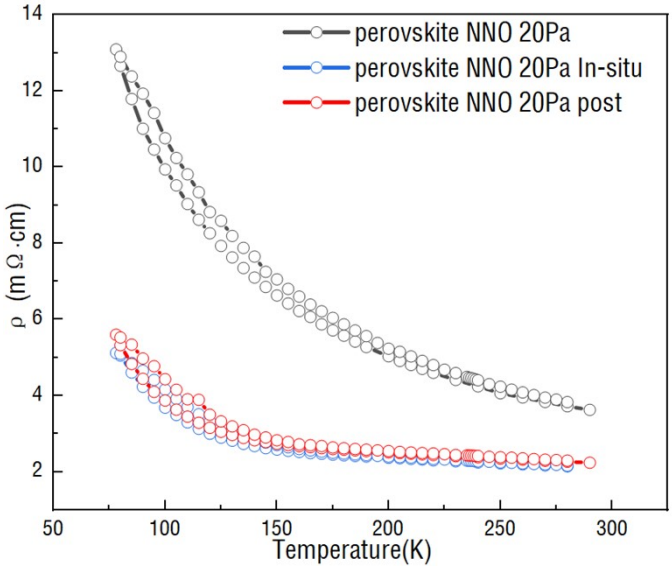

Figure S5 The change trend of R-T curves of perovskite $NdNiO_3$ films, under post-annealed, in-situ annealed methods.

As shown in Figure S5, the room temperature resistivity of perovskite $NdNiO_3$ grown on STO substrate decreased by 1.5 mΩ· cm after in-situ annealed and post annealed.

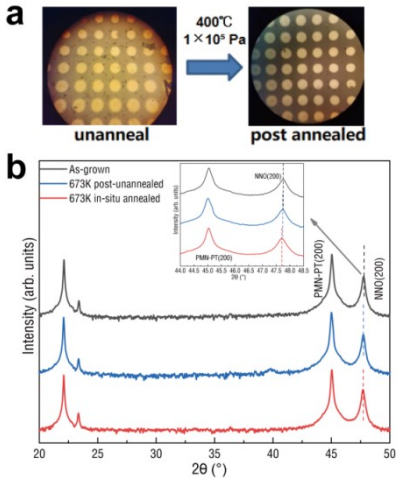

Figure S6 (a) The color change of sample surface after post-annealed at 673K. (b) The X-ray diffraction peaks, showing the (001) and (002) Bragg reflections of the R.P. $(NdNiO_3)_n$:NdO films deposited on a (001) PMN-PT single-crystal substrate. The inset shows the enlarged image of (002) peak.

The R.P. $(NdNiO_3)_n$:NdO films change from semitransparent to black after post-annealed at 673K. The X-ray diffraction peaks of R.P. $(NdNiO_3)_n$:NdO thin film did not shift significantly after in-situ annealed and post annealed.

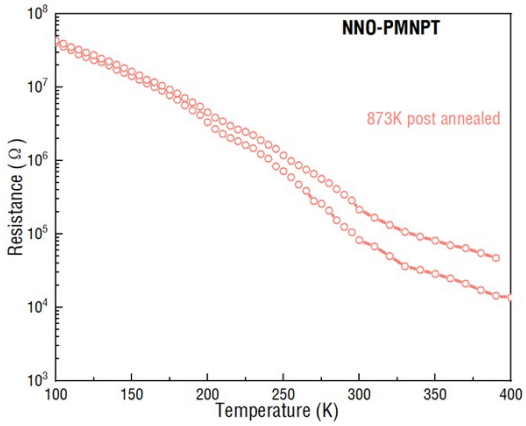

Figure S7 The R-T curves of R.P. $(NdNiO_3)_n$:NdO films under post-annealed at 873 K.

The R-T curve of the R.P. $(NdNiO_3)_n$:NdO film annealed at 873 K is shown in Figure S7. It can be seen that the metal insulator transition of the R.P. $(NdNiO_3)_n$:NdO film disappears when the post annealed temperature reaches 873 K.

Table S1 Comparison of the metal-insulator transition temperature T_{MIT} and $\Delta\rho$ with other heterostructures in previous studies.[1-7]

Materials	Metal-Insulator transition temperature T_{MIT}(K)	($\rho_{insulator}$ - ρ_{metal}) $\Delta\rho$ (Ω·cm)	References
NNO/STO-15 u.c.	150	1000	1
NNO/NGO-15 u.c.	150	10000	1
NNO/LSAT-15 u.c.	140	8000	1
NNO/STO-15 u.c.	150	4167	2
NNO/NGO-15 u.c.	150	125	2
NNO/LSAT-15 u.c.	140	5000	2
NNO/DSO-15 u.c.	120	3000	2
NNO/PMN-PT-65 u.c.	190	40.8	3
NNO/STO-100 u.c.	200	375	4
NNO/NGO-30 u.c.	150	8000	5
NNO/LAO-12 u.c.	100	20000	6
NNO/NGO-30 u.c.	155	200	7
NNO/LAO-12 u.c.	100	20000	7
NNO/KTO-30 u.c.	150	500	7
NNO/STO-30 u.c.	175	6250	7

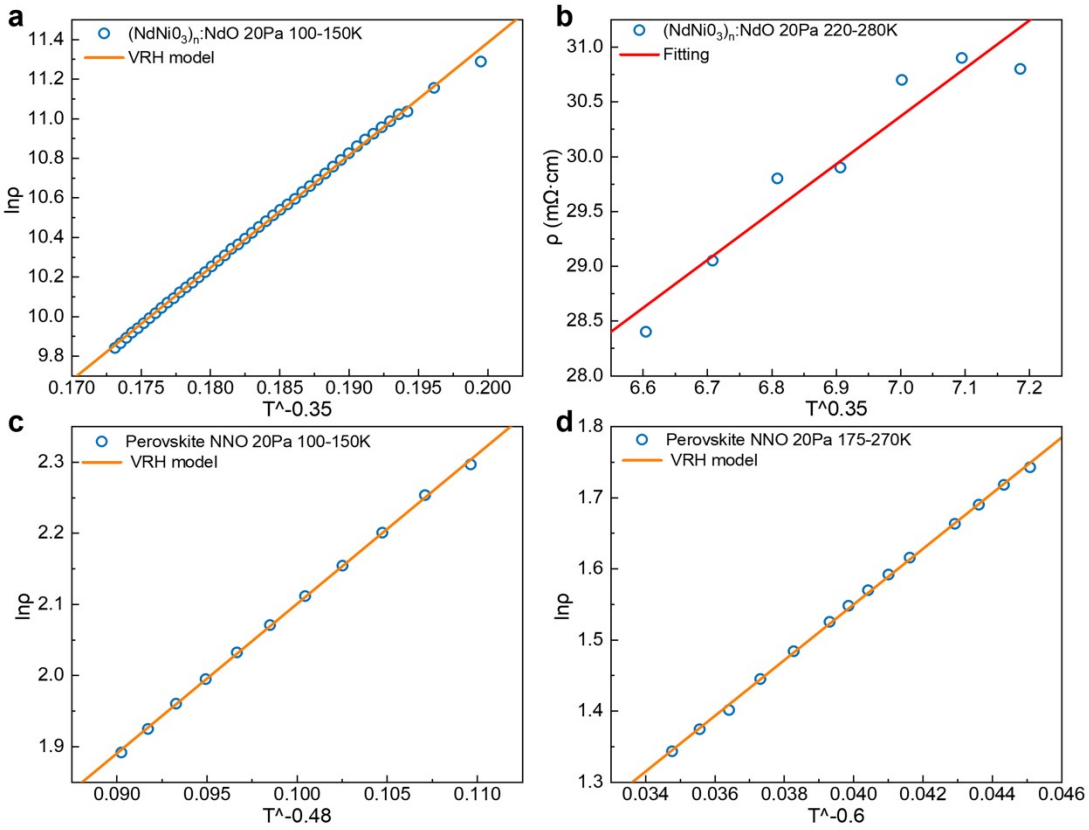

Figure S8 Resistivity of unannealed nickelate films as a function of T^n. Resistivity in the insulating phase (a) and metallic phase (b) of the R.P. $(NdNiO_3)_n$:NdO film as a function of temperature to the n-exponent. Resistivity in the insulating phase(c) and metallic phase(d) of the perovskite $NdNiO_3$ film as a function of temperature to the n-exponent.

It is important to pay attention to the extraction of the ρ (T) power law exponents from the experimental data. In order to extract these exponents, the experimentally obtained ρ (T) of each film was plotted as a function of T^n for different n values, all the different curves were fitted as linear fits as shown in fig. S8-10.

Within the measured temperature range, according to the Landau Fermi liquid model, when n=1, the system is a non Fermi liquid; When n=2, the system is a (Landau) Fermi liquid. By determining the value of the fitting parameter n, the degree of non Fermi behavior within the system can be semi quantitatively analyzed. The strength of non Fermi models is mainly characterized by the power exponent n. The strong correlation characteristics of d electrons are the main cause of non Fermi

transport behavior. The stronger the correlation, the closer the connection between electrons, and the slower the increase in resistivity caused by temperature rise. So, for systems with stronger correlations, the slower the rate of resistivity increase with temperature, the closer the index of the system is to 1. Conversely, for systems with weaker correlations, the faster the rate of resistivity increase with temperature, and the closer the index n of the system is to the power index 2 of Fermi liquids. Therefore, although the systems with $1<n<2$ belong to non Fermi liquid behavior, the strength of electron correlation within the system can be qualitatively determined by comparing the size of n.

As shown in fig S8-10, after in-situ annealed treatment, n value of perovskite $NdNiO_3$ thin film decreases to about 1/4, and at this time, the charge carriers in the film are dominated by the variable range hopping mechanism, and the thermal activation phonon scattering is weakened. After post annealed treatment, the n value did not change. When the temperature decreases, the insulation state n value of perovskite $NdNiO_3$ thin film increases to 0.66 after annealing. At this point, the film exhibits strong localization behavior using Mott VRH in the temperature range of 150 to 80 K. Meanwhile, the insulation state of the as-grown R.P. $(NdNiO_3)_n$:NdO film remained stable within the range of 1/4 after in-situ annealed and post annealed at 673K. unannealed R.P. $(NdNiO_3)_n$:NdO: The system belongs to non Fermi liquids, and as the temperature decreases, phonons can still provide sufficient energy within a larger temperature range. Electron conduction tends to coexist with the fixed range jump mode and the three-dimensional variable range jump mode, with n=0.35. The in-situ annealed R.P. $(NdNiO_3)_n$:NdO: the system transitions from non Fermi liquid to Fermi liquid, but still belongs to non Fermi liquid, coexisting with the metal transport and interband electron transition of the system, where n=1.26; The post-annealed R.P. $(NdNiO_3)_n$:NdO: The system exhibiting a Non-Fermi liquid behaviour with a power-law exponent reaching of 2.75. The power law exponent of perovskite $NdNiO_3$ is always below 1 and fluctuates around 1/4.

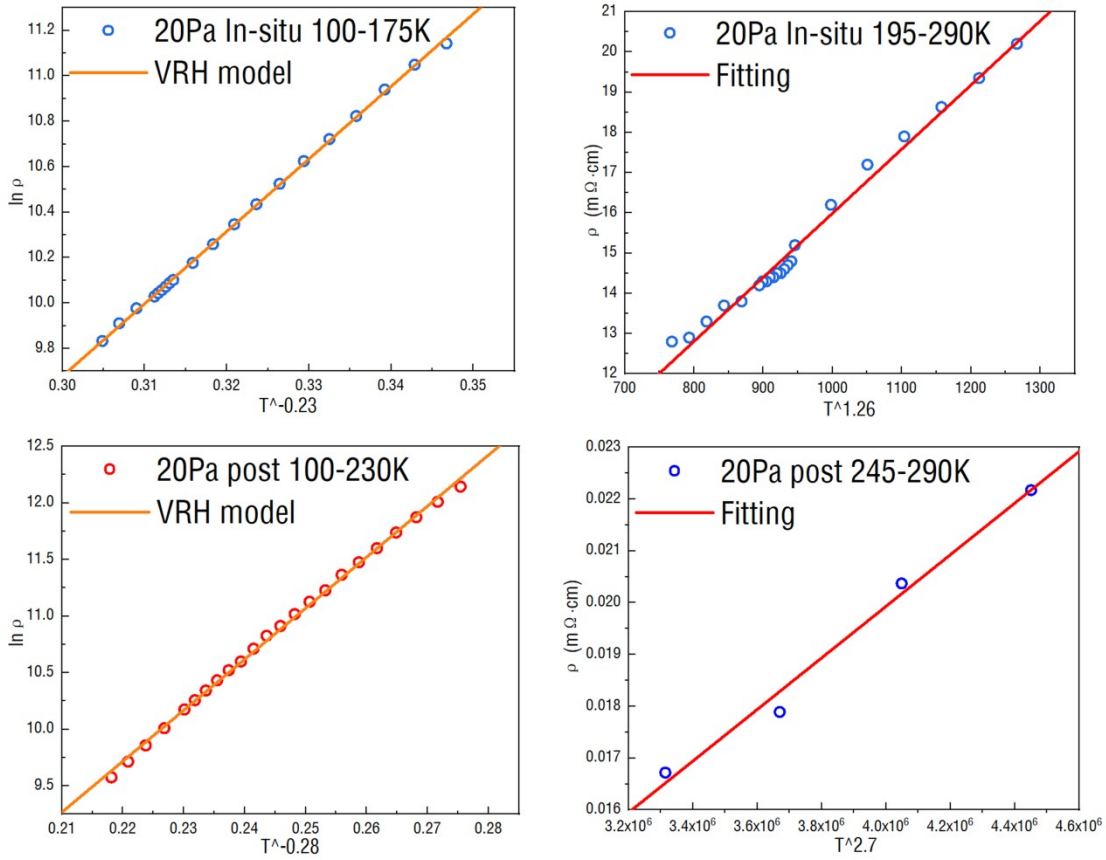

Figure S9 Resistivity of annealed R.P. $(NdNiO_3)_n$:NdO films as a function of T^n. Resistivity in the insulating phase (a) and metallic phase (b) of the in-situ annealed R.P. $(NdNiO_3)_n$:NdO film as a function of temperature to the n-exponent. Resistivity in the insulating phase(c) and metallic phase(d) of the post annealed R.P. $(NdNiO_3)_n$:NdO film as a function of temperature to the n-exponent.

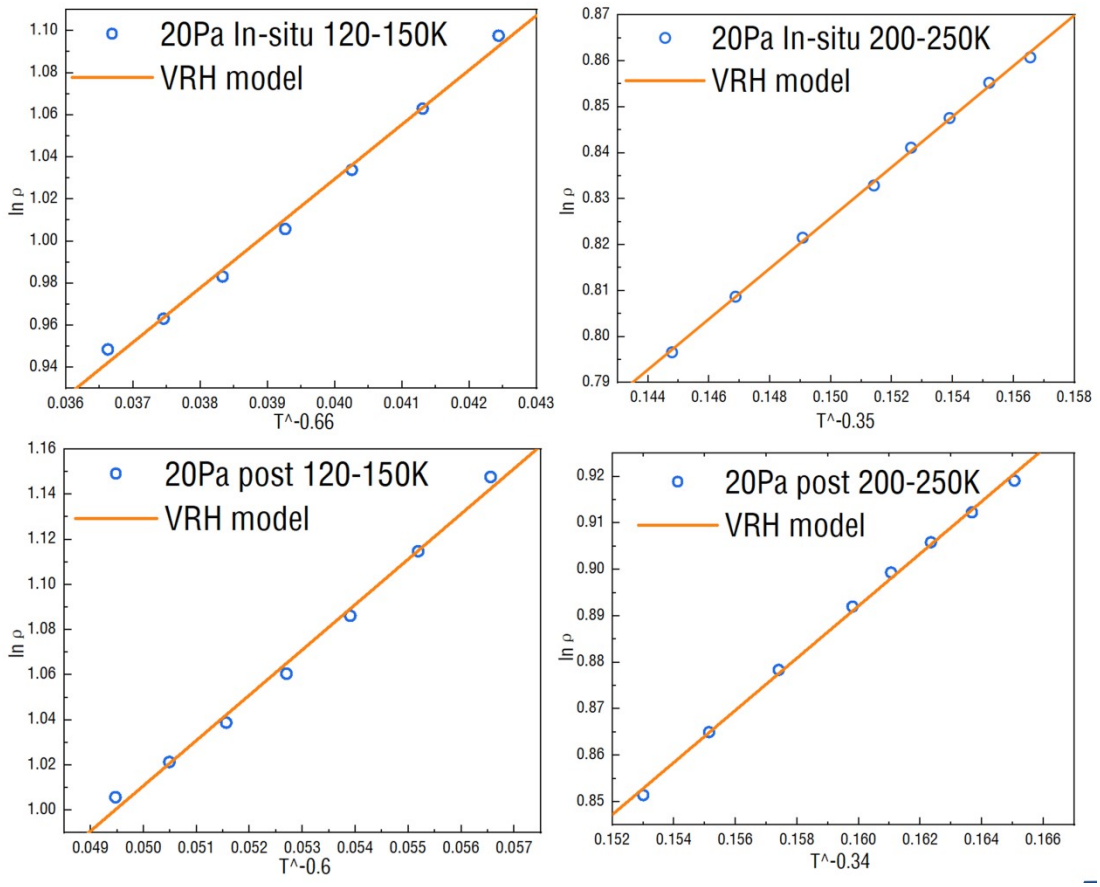

Figure S10 Resistivity of annealed perovskite $NdNiO_3$ films as a function of T^n. Resistivity in the insulating phase (a) and metallic phase (b) of the in-situ annealed perovskite $NdNiO_3$ film as a function of temperature to the n-exponent. Resistivity in the insulating phase(c) and metallic phase(d) of the post annealed perovskite $NdNiO_3$ film as a function of temperature to the n-exponent.

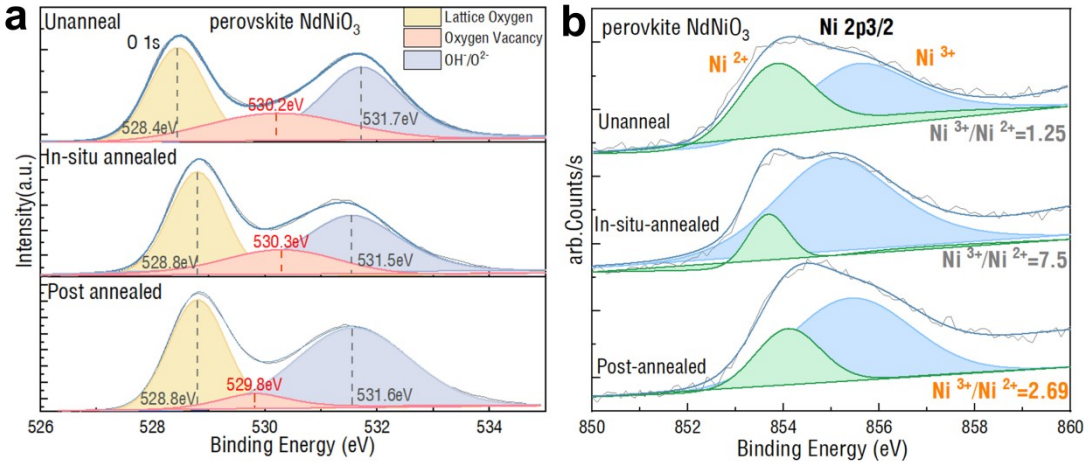

Figure S11 X-ray photoelectron spectroscopy (XPS) of perovskite $NdNiO_3$ films on $SrTiO_3$ substrate. The grey line is the test data, the blue line is the fitting data, and the solid line is the peak data. The (a) O 1s and Ni *2p* XPS spectra of perovskite $NdNiO_3$ films under different

annealed methods.

The Ni 2p3/2 peak essentially overlap at ~854 eV. This set of spectra demonstrates there is 0.5 eV chemical shift in the Ni 2p 3/2 peak (~855.5 eV) after annealed methods, confirming the variant oxidation state of Ni^{3+}. The ratio of Ni^{3+}/Ni^{2+} first increases to 7.5 and then decreases to 2.69 accompanying with the different annealed methods.

Table S2 The comparison specific peaks of O, Ni and Nd ions for perovskite $NdNiO_3$ and R.P. $(NdNiO_3)_n$:NdO samples at RT, respectively.The number in the first row of each cell in Table S2 represents Binding Energy, while the number in the second row represents the element content.

	situation	Ni^{3+}	Ni^{2+}	Ni^{3+}/Ni^{2+}	Lattice oxygen	Oxygen vacancy	OH^-/O^{2-}
Layered $(NdNiO_3)_n$: NdO	as-grown	855.3 15000	853.8 9000	1.67	528.5 26154	530.0 13721	531.7 41988
	In-situ annealed	854.9 22000	853.5 5000	4.4	528.5 21525	530.0 5796	531.2 32439
	post annealed	855.1 23727	853.6 10520	2.26	528.4 32167	529.7 12430	531.3 70962
Perovskite $NdNiO_3$	as-grown	855.5 15000	853.8 12000	1.25	528.4 27884	530.2 20102	531.7 37486
	In-situ annealed	855.0 30000	853.67 4000	7.5	528.8 25155	530.3 12622	531.5 33525
	post annealed	855.4 19948	854.1 7420	2.69	528.8 41450	529.8 11458	531.6 66490

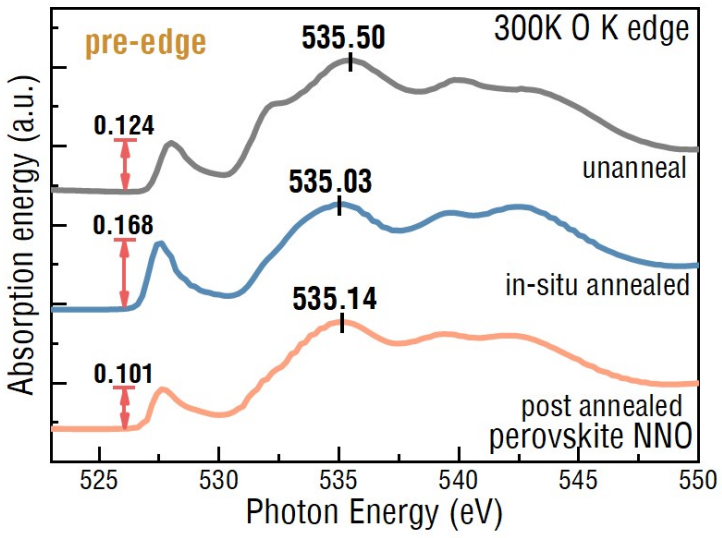

Figure S12 X-ray absorption spectroscopy (XAS) of $NdNiO_3$ films on $SrTiO_3$ substrate at 300K.

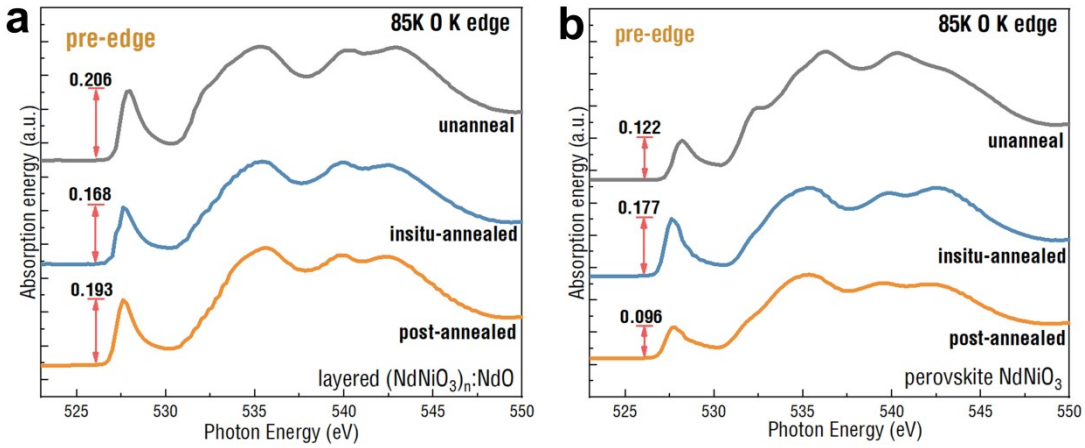

Figure S13 X-ray absorption spectroscopy (XAS) of R.P. $(NdNiO_3)_n$:NdO and perovskite $NdNiO_3$ films at 85K.

In the calculation of $NdNiO_3$ structures, we constructed a 2×1×2 supercell, taking into account all the possible magnetic configurations: ferromagnetic (FM), E-type, N-type, S-type, and T-type antiferromagnetic (AFM) states (see Fig. SX1). As shown in Table S3, in both perovskite $NdNiO_3$ (2.57% tensile strain) and $(NdNiO_3)_n$:NdO (5.65% tensile strain) films, the magnetic ground state of $P2_1/n$ $NdNiO_3$ is AFM-S with an out-of-plane magnetic moment. The AFM-S state has a band gap of 0.5 eV (Figure 4b), which is consistent with the experimental result[8]. On the other hand, the *Pnma* structure of $NdNiO_3$, which may also exist in the perovskite $NdNiO_3$ and $(NdNiO_3)_n$:NdO films, favors a metallic FM state with the total energy being lower than that of AFM phases (E, N, S, and T types) by more than 200 meV per unit cell (Table S3).[9-10] The coexistence of AFM-S semiconducting phase and metallic FM phase in $NdNiO_3$ structures give rise to several-hundred Ω resistance of perovskite $NdNiO_3$ as shown in Figure 1c. Note that the electronic structures nearby Fermi level hardly change with the tensile strain (Figure 4b), showing that the dramatic variation of electronic resistance observed in R.P. $(NdNiO_3)_n$:NdO (Figures 1c and 2a) is not originated from the $NdNiO_3$ structure.

Then we further explored the effect of newly appeared Nd_2NiO_4 structure ($\sigma = 0$) on the electronic transport property of R.P. $(NdNiO_3)_n$:NdO films. As shown in Table S4, all the three possible Nd_2NiO_4 structures, i.e., Bmab, P42-ncm, and Pccn

structures, were considered in our calculations. Since the Nd_2NiO_4 has a collinear magnetic structure,[11] the FM, A-type and G-type AFM states were considered in each structure (Figure S15). It is found that the AFM-G state is at least 630 meV per unit cell more stable than other magnetic states in all the three Nd_2NiO_4 structures (Table S4). We additionally calculated the electronic structures of AFM-G state. As shown in Figure 4c, there is a large insulating band gap of 1.7 eV in all the three Nd_2NiO_4 structures, which is much larger than that of $NdNiO_3$ structures. This result shows that the appearance of intrinsic R. P. phase in $(NdNiO_3)_n$:NdO films has an effect enhancing electric resistance, which agrees our the experimental observation as shown in Figure 1c.

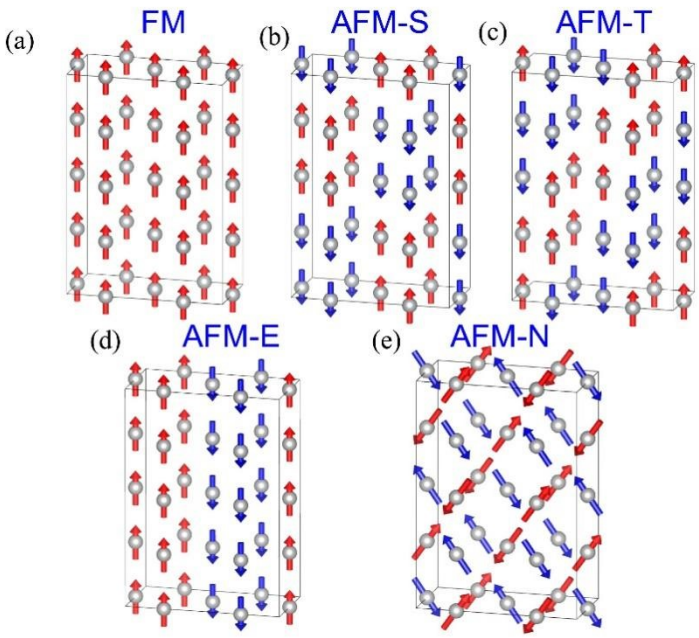

Figure S14. (a) Ferromagnetic (FM), (b) S type antiferromagnetic (AFM-S), (c) T type antiferromagnetic (AFM-T), (d) E type antiferromagnetic (AFM-E), and (e) N type antiferromagnetic (AFM-N) configurations in $NdNiO_3$. Arrows represent the directions of spin moments on the Ni atoms.

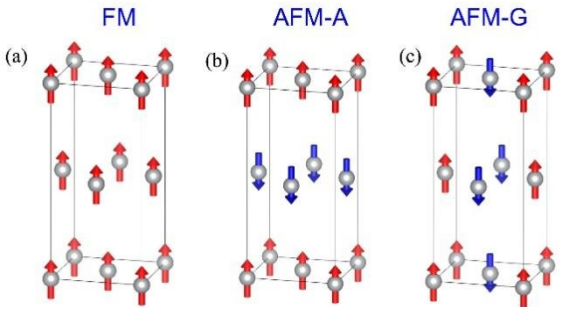

Figure S15. (a) Ferromagnetic (FM), (b) A type antiferromagnetic (AFM-A), and (c) G type antiferromagnetic (AFM-G) configurations in Nd_2NiO_4. Arrows represent the directions of spin moments on the Ni atoms.

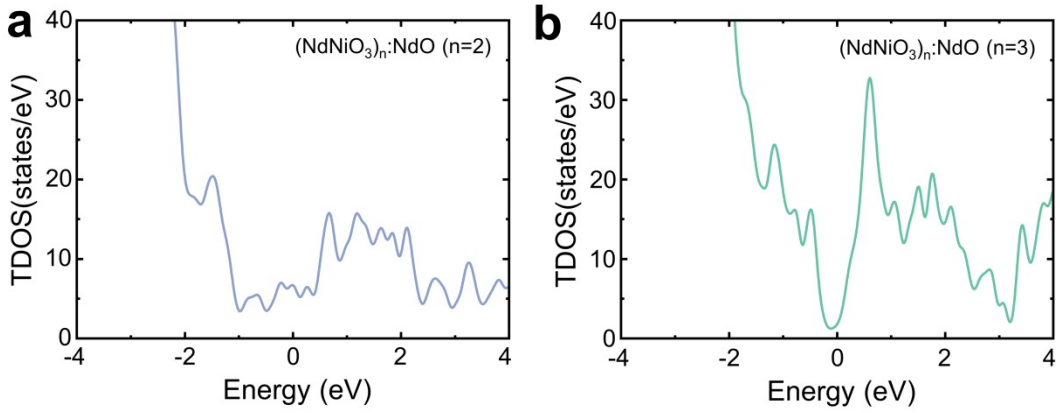

Figure S16. Calculated total density of states (TDOS) of $(NdNiO_3)_n$:NdO layers. (a) is for n = 2, (b) is for n = 3, respectively.

Figure S16 shows the total density of states (TDOS) of $(NdNiO_3)_n$:NdO layers. It is found that the G-AFM phase of n = 1 structure has a large band gap showing the nature of insulator. Whereas, both the A-AFM phase of n = 2 structure and FM phase of n = 3 structure have zero band gap, showing a metallic character.

Table S3. Calculated total energies of $NdNiO_3$ with different magnetic structures, which are defined relative to that of the AFM-S and FM states for $P2_1/n$ and Pnma phase, respectively.

	(meV)	FM	AFM-S	AFM-T	AFM-E	AFM-N
2.57 % ($P2_1/n$)	Without-SOC	155.58	0.00	21.84	35.62	——
	With-SOC	——	0.00(M//z)		——	0.49
2.57 % (Pnma)	Without-SOC	0.00	——	459.38	——	——
	With-SOC	0.00(M//x)	600.52	——	227.09	578.48
5.65 % ($P2_1/n$)	Without-SOC	84.73	0.00	40.42	4.17	——
	With-SOC	——	0.00(M//z)	——	——	0.85
5.65 % (Pnma)	Without-SOC	0.00	——	266.84	——	——
	With-SOC	0.00(M//z)	343.91	——	199.50	336.24

Table S4. Calculated total energies of Nd_2NiO_4 with different magnetic structures, which are defined relative to that of the AFM-G state.

meV	FM	AFM-A	AFM-G
Bmab-5.65 %	630.00	——	0.00
P42-ncm-5.65 %	687.98	690.70	0.00
Pccn-5.65%	687.25	689.93	0.00

Table S5. Formation energy E_f for $Nd_2NiO_{4+\delta}$.

	Bmab	P42/ncm	Pccn
eV	-5.89950	-4.99510	-5.54552

Table S6. Calculated total energies of $Nd_2NiO_{4+\delta}$ different magnetic structures, which are defined relative to that of the FM state.

meV	FM	AFM-A	AFM-G
Bmab-5.65 %	0.00	0.82	293.73
P42-ncm-5.65 %	0.00	11.55	108.29
Pccn-5.65%	0.00	0.82	293.46

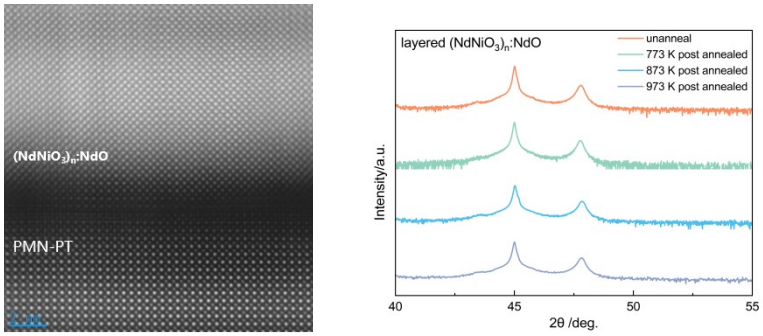

Figure S17. The STEM image of Ruddlesden-Popper $(NdNiO_3)_n$:NdO samples after post-annealed at 973 K. (b) The XRD datas of before and after post-annealed process.

The annealing temperatures is up to 973 K, the corresponding TEM image as follow in Figure S17, and there is no the lattice degradation. And, it is difficult to observe the intercalated oxygen ions due to the disordered distribution after the annealing process. The result also keeps consistent with the corresponding XRD data.

References

[1] Evgeny Mikheev et al. ,Tuning bad metal and non-Fermi liquid behavior in a Mott material: Rare-earth nickelate thin films.Sci. Adv.1,e1500797(2015).

[2] Liu, J., Kargarian, M., Kareev, M. et al. Heterointerface engineered electronic and magnetic phases of NdNiO3 thin films. Nat Commun 4, 2714 (2013).

[3] Yan, J.-M., et al. Manipulation of the Electronic Transport Properties of Charge-Transfer Oxide Thin Films of $NdNiO_3$ Using Static and Electric-Field-Controllable Dynamic Lattice Strain. Physical Review Applied 11(3): 034037. (2019)

[4] Guo, Q., Farokhipoor, S., Magén, C. et al. Tunable resistivity exponents in the metallic phase of epitaxial nickelates. Nat Commun 11, 2949 (2020).

[5] Mattoni, G., Zubko, P., Maccherozzi, F. et al. Striped nanoscale phase separation at the metal–insulator transition of heteroepitaxial nickelates. Nat Commun 7, 13141 (2016).

[6] Preziosi D, Lopez-Mir L, Li X, Cornelissen T, Lee JH, Trier F, Bouzehouane K, Valencia S, Gloter A, Barthélémy A, Bibes M. Direct Mapping of Phase Separation across the Metal-Insulator Transition of $NdNiO_3$. Nano Lett. 2018 Apr 11;18(4):2226-2232.

[7] Scherwitzl, R., Zubko, P., Lezama, I.G., Ono, S., Morpurgo, A.F., Catalan, G. and Triscone, J.-M. (2010), Electric-Field Control of the Metal-Insulator Transition in Ultrathin $NdNiO_3$ Films. Adv. Mater., 22: 5517-5520.

[8] D. I. Badrtdinov, A. Hampel, C. E. Dreyer. Interplay between breathing-mode distortions and magnetic order in rare-earth nickelates from ab initio magnetic models. Physical Review B 104, 054403 (2021).

[9] J. Rodruguez-Carvajal, M. T. Fernandez-Diaz, J. L. Martinez, F. Fernandez, R. Saez-Puche. Structural phase-transitions and 3-dimensional magnetic-ordering in the Nd2NiO4 oxide. Europhysics Letters 11, 261 (1990).

[10] G. Kresse, J. Hafner. Ab initio molecular dynamics for liquid metals. Physical Review B 47, 558 (1993).

[11] G. Kresse, D. Joubert. From ultrasoft pseudopotentials to the projector augmented-wave method. Physical Review B 59, 1758 (1999).